IOP Publishing Nanotechnology
Nanotechnology 33 (2022) 015001 (9pp) https://doi.org/10.1088/1361-6528/ac2b71

Nanoscale axial position and orientation measurement of hexagonal boron nitride quantum emitters using a tunable nanophotonic environment

Pankaj K Jha[1,4], **Hamidreza Akbari**[1,4], **Yonghwi Kim**[1,4], **Souvik Biswas**[1] and **Harry A Atwater**[1,2,3,*]

[1] Thomas J. Watson Laboratory of Applied Physics and Materials Science, California Institute of Technology, Pasadena, CA 91125, United States of America
[2] Resnick Sustainability Institute, California Institute of Technology, Pasadena, CA 91125, United States of America
[3] Joint Center for Artificial Photosynthesis, California Institute of Technology, Pasadena, CA 91125, United States of America

E-mail: haa@caltech.edu

Received 3 June 2021, revised 22 September 2021
Accepted for publication 29 September 2021
Published 20 October 2021

Abstract

Color centers in hexagonal boron nitride (*h*BN) have emerged as promising candidates for single-photon emitters (SPEs) due to their bright emission characteristics at room temperature. In contrast to mono- and few-layered *h*BN, color centers in multi-layered flakes show superior emission characteristics such as higher saturation counts and spectral stability. Here, we report a method for determining both the axial position and three-dimensional dipole orientation of SPEs in thick *h*BN flakes by tuning the photonic local density of states using vanadium dioxide (VO_2), a phase change material. Quantum emitters under study exhibit a strong surface-normal dipole orientation, providing some insight on the atomic structure of *h*BN SPEs, deeply embedded in thick crystals. Next, we optimized a hot pickup technique to reproducibly transfer the *h*BN flake from VO_2/sapphire substrate onto SiO_2/Si substrate and relocated the same emitters. Our approach serves as a practical method to systematically characterize SPEs in *h*BN prior to integration in quantum photonics systems.

Supplementary material for this article is available online

Keywords: hBN, vanadium dioxide, quantum emitter, hexagonal boron nitride

(Some figures may appear in colour only in the online journal)

Introduction

Over the past few decades, point defects [1] that introduce electronic states with optical transitions, also known as color centers, have garnered great interest for quantum photonics applications, such as quantum computation and quantum information [2, 3], quantum cryptography [4], and quantum sensing [5]. Wide-bandgap materials, such as diamond [6], silicon carbide [7], gallium nitride [8], and zinc oxide [9] offer promising platforms for hosting quantum emitters with emission in the visible to near-infrared spectrum. However, these materials suffer from one or more intrinsic challenges such as a requirement for cryogenic temperatures, decoherence of emitted photons, optical coupling losses, and challenges associated with chip-based photonic integration.

[4] These authors contributed equally to this work.
[*] Author to whom any correspondence should be addressed.

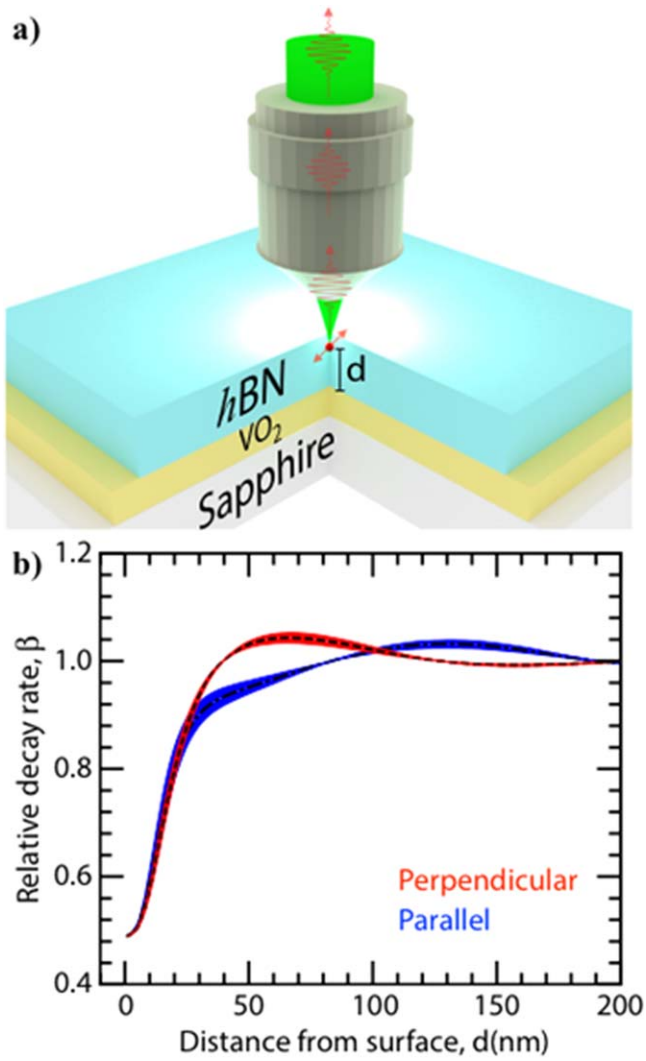

Figure 1. Experimental schematic and distance-dependent modulation of relative decay rates. (a) Schematic of a quantum emitter in an atomically thin crystal of hexagonal boron nitride (*h*BN) located within the thickness of a flake on a substrate which consists of a thin layer of vanadium dioxide (VO_2) deposited on a sapphire crystal. (b) Relative decay rate $\beta = \gamma_{Insulating}/\gamma_{Metallic}$ as a function of distance d of a quantum emitter from the surface of VO_2 when switched from the insulating to metallic state. The blue and red curves refer to quantum emitters oriented parallel and perpendicular to the surface respectively and the shaded regions corresponds to the typical quantum yield (QY) range of 0.6–1.0 of *h*BN quantum emitters with zero-phonon line around 600 nm [41]. For numerical simulation we considered the emission wavelength of 600 nm for the quantum emitter corresponding to the emitter 'A' (figure 2(e)). The dashed line within the shaded region corresponds to QY = 0.79 as estimated from our experimental data (supplementary Sec. S2). The refractive indices of the upper medium, *h*BN, and that of sapphire were set to 1, 1.82 [42], and 1.77 [43] respectively. The refractive index of VO_2 at 600 nm was set to 3.05 + 0.42i (insulating state) and 2.57 + 0.64i (metallic state) from our ellipsometric data (supplementary figure S1).

These problems have driven researchers to seek new candidate materials with fewer disadvantages [10, 11].

Recent discoveries of quantum light emission from two-dimensional van der Waals (vdW) layered materials [12–17] have introduced promising candidates for single photon emitters (SPEs). In contrast to bulk materials, vdW materials offer easier integration with photonic structures and minimal loss due to refractive index mismatch [18, 19]. Among several candidate vdW host materials, hexagonal boron nitride (*h*BN) has received particular attention due to its ability to offer a bright source of quantum light at room temperature. Remarkably, quantum emitters in *h*BN have shown high (> 80%) Debye–Waller factor [17], a brightness comparable to the brightest SPEs [10, 19], polarized emission [17, 20], giant stark shift [21–23], magnetic-field dependent quantum emission [24, 25], correlated cathodoluminescence and photoluminescence emission [26], and near transform-limited optical linewidth [27], all reported at room temperature. To this date, the atomic structure of *h*BN quantum emitters is not clear; the most common approach to deduce the atomic structure of these emitters has been to compare the energy of the zero-phonon line (ZPL) and phonon-assisted emission to the first-principles calculations [28]. Furthermore, to understand and quantify the intricate details of the emitter atomic structure, in particular spin-manifold, optically detected magnetic resonance technique has been recently reported [25]. Accurate information of three-dimensional (3D) orientation of emitting dipole would provide invaluable insight into the underlying symmetry properties of the defect center, which can complement the aforementioned approaches and help in identifying the atomic origin of emitters.

Quantum emitters in multi-layered flakes, in contrast to mono- and few-layered flakes, show superior emission characteristics such as higher saturation counts and spectral stability due to reduced environmental screening effects [29]. Efficient coupling of these quantum emitters with nanophotonic structures would require precise information about their axial position and 3D dipole orientation. Determining, both, the 3D dipole orientation and axial position of a quantum emitter in any multi-layered *h*BN poses as a coupled problem because the polarization characteristics of detected photons is strongly influenced by either dipole orientation or axial position.

In this Letter, we demonstrate nanometer-scale axial location of *h*BN quantum emitters in a multi-layered flake by leveraging highly sensitive, distance-dependent modulation of the spontaneous emission lifetime of these quantum emitters when in close proximity to a tunable phase-change material, vanadium dioxide (VO_2). Specifically, we modify the local density of optical states (LDOS) by inducing an insulator-to-metal transition in VO_2 which in turn modulates the emission rate of quantum emitters near the *h*BN/VO_2 interface. This method, taken together with emission polarimetry to determine the 3D orientation of the quantum emitter, gives comprehensive information about emitters axial position and orientation, which could be used to distinguish possible candidates based on atomic structure of the emitter. Furthermore, we have optimized a polymer-assisted hot pickup and transfer process to reliably transfer *h*BN flakes from VO_2 substrate onto other device substrates (here, we use SiO_2/Si substrate as target), following which, the emitters under investigation were relocated. Measurement of *h*BN emitter location and 3D orientation with nanometer-scale resolution

in multi-layered flakes together with advances in precise transfer and stacking of 2D materials [30] and metal contacts [31] offer opportunities for both fundamental physics advances [32] and quantum photonic technologies [33, 34].

Results and discussions

The experimental configuration is shown in figure 1(a). A quantum emitter is located at a distance d, within the thickness of an hBN flake, from the surface of a substrate that consists of a thin layer of VO_2 on sapphire. Photoluminescence excitation and detection were performed with optical pumping of quantum emitters by laser excitation from the top. The excitation wavelength was set to 532 nm. The excited quantum emitter emission decay rate depends on its interaction with the optical environment [35]. By optical environment we mean the substrate beneath and the air above the hBN flake. We model this interaction by treating the quantum emitter as an oscillating point dipole source oriented along the direction (θ, φ). For an emitter in an unbounded, homogeneous, and lossless medium with a refractive index n, the spontaneous decay rate is enhanced by a factor n compared to the free space. This result also holds true for bounded geometry as long as the emitter is at a distance $d \gg \lambda$ from any interface. When $d \ll \lambda$ the decay rate strongly depends on d, the dipole orientation (θ, φ), and the refractive index contrast across the interface [36–39]. In this work, we manipulated the optical environment of a quantum emitter located in the vicinity of the hBN/VO_2 interface using VO_2 whose complex refractive index exhibits a sharp change when VO_2 is thermally switched from the insulating to metallic state, which occurs at near room temperature $T_c \sim 340$ K [40].

Figure 1(b) shows the calculated relative decay rate $\beta = \gamma_{Insulating}/\gamma_{Metallic}$ of an emitter as a function of distance d when the emitter is oriented perpendicular ($\theta = 0°$) and parallel ($\theta = 90°$) to the hBN/VO_2 interface. Here, $\gamma_{Insulating}$ and $\gamma_{Metallic}$ is the total (radiative and non-radiative) decay rate of the emitter when VO_2 is in insulating (30 °C) and metallic (100 °C) state respectively. In these simulations, we considered a flake thickness of 310 nm (as shown in figure 2(c)) and an emission wavelength of 600 nm, corresponding to one of the quantum emitters in our experiment, shown in figures 2(d) and (e). The refractive indices of the upper medium, hBN, and that of sapphire were set to 1, 1.82 [44], and 1.77 [37] respectively. The complex refractive index of VO_2 at 600 nm was extracted from our ellipsometric data and was set to 3.05 + 0.42i and 2.57 + 0.64i for VO_2 in insulating and metallic state respectively (supplementary section S1 (available online at stacks.iop.org/NANO/33/015001/mmedia)). The thickness of the VO_2 layer on sapphire was set to 40 nm (supplementary section S1). In general, the photoluminescence quantum yield (PLQY) of hBN quantum emitters varies in the range 0.6–1.0 [10, 19] and a recent experiment has shown average PLQY in the range 0.6–0.8 for quantum emitters with ZPL around 600 nm [41]. The shaded area in figure 1(b), corresponds to this PLQY range. The dashed line within the shaded regions corresponds to a PLQY = 0.79 estimated from our experimental data (supplementary section S4). As can be seen in our simulation results, the relative modulation of decay rates for both orientations is clearly evident within first ~50 nm that quickly fades away at distances ~100 nm and above. We use this highly sensitive, distance-dependent decay rate of quantum emitters in the vicinity of the hBN/VO_2 interface to localize their position along the axial direction.

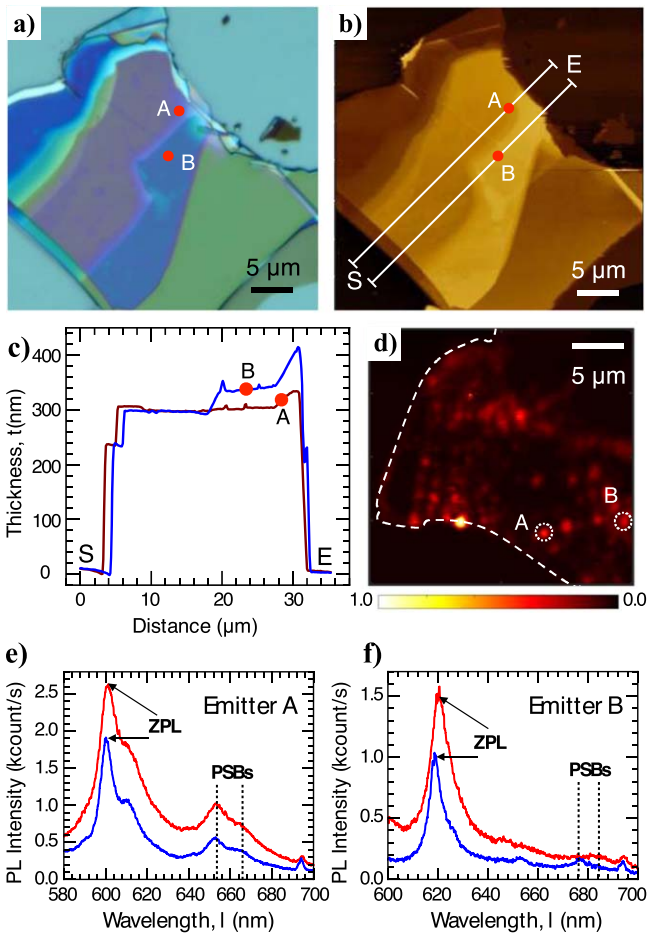

Figure 2. Characterization of the exfoliated flake and spectra of hBN quantum emitters. (a) Optical image of the mechanically exfoliated hBN flake on VO_2/sapphire substrate. (b) Atomic force microscopy image of the flake shown in (a). The red dots on the traces (S-E) in (b) and (a) indicate the position of emitters 'A', and 'B' with emission wavelength of 600 nm and 620 nm, respectively. (c) Line profiles along the region indicated by the trace in (b). At the location of the emitter 'A' and 'B' height of the flake is 310 nm and 340 nm respectively. (d) Confocal photoluminescence (PL) map of the hBN flake. The position of two single photon emitters is marked by white circles. The edge of the flake in marked by white dashed line. The PL spectra of emitters 'A' and 'B' shown in (e) and (f) respectively were obtained with VO_2 in insulating state (blue) and metallic state (red). In these spectra ZPL and phonon sidebands (PSBs) are highlighted and the small peak around 692 nm corresponds to the emission from sapphire.

Figure 2(a) shows the optical microscope image of a thin hBN flake on a VO_2/sapphire substrate. This sample was prepared by mechanical exfoliation of high purity hBN single crystals and transferred onto a 40 nm thick VO_2 film

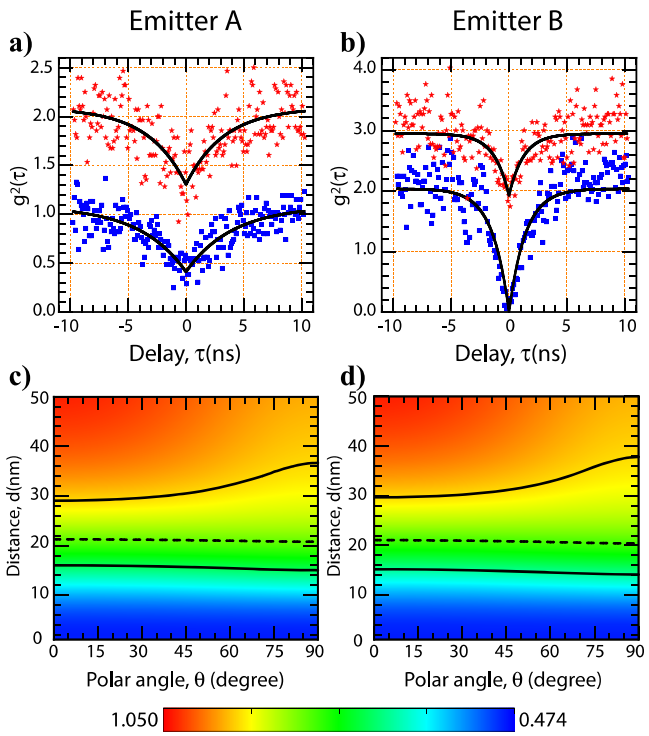

Figure 3. Single photon source characterization and axial location in *h*BN flake. Plot of the second order photon correlation measurement, $g^2(\tau)$ for the emitters 'A' and 'B', in (a) and (b) respectively. The experimental data, blue squares for insulating VO_2 phase and red stars for metallic VO_2, were fitted using equation (1) to obtain the decay rates of the emitters. From the fit, we calculated the relative decay rates $\beta = \gamma_{Insulating}/\gamma_{Metallic}$ for the three emitters 'A' and 'B' as 0.818 ± 0.108 and 0.800 ± 0.124 respectively. For clarity, $g^2(\tau)$ data obtained for metallic VO_2 in (a), and (b) were shifted by 1 and 1.5 respectively. Plot of the relative decay rates β as a function of the distance (d) from the surface of VO_2 and the polar angle (θ) for the emitters 'A' and 'B' are shown in (c) and (d) respectively. The dashed contour lines in (c) and (d) corresponds to the experimental value of β obtained from (a) and (b) respectively, while the solid lines correspond to the error ($\pm\Delta\beta$) in the ratio.

deposited on 500 μm thick sapphire by pulsed laser deposition. To determine the thickness of this flake at each position, we employed atomic force microscopy (AFM). Figure 2(b) shows an AFM image of the *h*BN flake shown in figure 2(a). The red dot in figures 2(a) and (b) indicates the location of the quantum emitters 'A' and 'B' with emission wavelength of 600 nm and 620 nm, respectively. Figure 2(c) show AFM height profile across the lines (S-E) indicated in figure 2(b) where flake thickness varies in the range 230–420 nm. At the location of the emitter 'A' and 'B' height of the flake is 310 nm and 340 nm respectively.

To locate the quantum emitters precisely, we performed confocal photoluminescence (PL) mapping in mode by which the sample was scanned point by point. Figure 2(d) shows a PL map over an area of 20×20 μm^2 on the *h*BN flake. The location of the quantum emitters 'A' and 'B' are highlighted by dashed circles. The single photon emission nature of these quantum emitters is evident from their second-order auto-correlation measurements indicating $g^2(0) < 0.5$ (see figures 3(a) and (b)). Figures 2(e) and (f) show the PL spectra of these quantum emitters obtained for insulating and metallic VO_2. The emission spectra of each quantum emitter consist of a pronounced ZPL accompanied by a weaker phonon assisted emission [10, 17, 45]. An increase in PL intensity as obtained for metallic VO_2 compared to insulating VO_2 is noticeable for all quantum emitters, which in general suggests a higher photon emission rate i.e. a decrease in emission lifetime, a change in illumination pattern, or any of these. However, in our experiments, a decrease in the emitter lifetime obtained from Hanbury Brown and Twiss (HBT) measurements for metallic VO_2 compared to insulating VO_2 suggests that this increase in absolute PL intensity originates from enhancement of emission rate. Recent experiment has reported that the decay rate of *h*BN quantum emitters remains constant even when heated up to 800 K [46] which further corroborates that the enhancement of decay rate is due to modification in LDOS rather than a thermal effect. The defect-based quantum emitter dimensions are at the atomic scale, and thus the lateral position can be precisely measured down to few tens of nm when a sufficient number of photons is collected by the camera along with low noise (readout and amplification) and background signals.

To investigate the single-photon emission characteristics and decay lifetime of the quantum emitters, we measured their second-order intensity correlation functions $g^2(\tau)$ in both insulating and metallic phases of VO_2. In order to reduce the influence of background signal and noise, we corrected the raw $g^2_{raw}(\tau)$ using the function $g^2(\tau) = [g^2_{raw}(\tau) - (1 - \rho^2)]/\rho^2$, where $\rho = S/(S + B)$ where S and B refer to the signal and the background counts, respectively. This background corrected $g^2(\tau)$ was fitted with double exponential of the form [20]

$$g^2(\tau) = 1 - \rho^2[(1 + \zeta)e^{-\gamma_1|\tau|} - \zeta e^{-\gamma_2|\tau|}], \qquad (1)$$

where, ζ, ρ, $\gamma_{1,2}$ are laser power-dependent parameters [20, 47]. Here, γ_1 and γ_2 are the faster and the slower decay time constants, respectively, for a three-level system. The second-order intensity correlation functions $g^2(\tau)$ under continuous wave excitation pumping for the quantum emitters 'A' and 'B' is shown in figures 3(a) and (b) respectively, when VO_2 is insulating (blue dots) and metallic phase (red dots). The data for the metallic phase VO_2 configuration has been offset vertically for visual clarity. Equal-time coincidence counts $g^2(0)$ for each quantum emitter is less than 0.5, which indicates the presence of a single emitter. All measurements were performed at a constant 50 μW pump laser power which is orders of magnitude smaller compared to the saturation power of $\sim$ mW for *h*BN quantum emitters [10, 18, 19]. Given the Fresnel reflections from all interfaces, which were analyzed using full-wave simulations, the excitation power within the flake along the axial direction is position dependent. From fitting our experimental data of correlation functions $g^2(\tau)$, we extracted the decay constants ($\gamma_{1,2}$) which has contributions from the spontaneous decay rates and the pump rate [48, 49]. The spontaneous decay rates (γ) of the emitters 'A' and 'B' are shown in the Table T1 (see supplementary information section S2 for details). The correlation functions over long-time scales are shown in figure S10. With an excitation power of 50 μW,

the pump rates are $\sim$ 25-fold and 73-fold slower than the spontaneous decay rates for emitters 'A' and 'B', respectively, and thus make negligible contributions to the decay constants. From Table T1, we clearly see that for all the emitters, the decay rates are higher in the presence of a metallic-VO_2 when compared to an insulating-VO_2 configuration. Thus, the emitters 'A' and 'B' are located at distances, from the surface of VO_2, such that their optical environment is modified when VO_2 undergoes an insulator-to-metal transition.

To model the distance-dependence of the quantum emitter lifetime on VO_2 phase, we define the ratio of their decay rates in the insulating and metallic phases as β. Figures 3(c) and (d) show the two-dimensional plot of relative decay rate β as a function of distance d from the hBN/VO_2 interface and the polar orientation angle θ of the dipole for each quantum emitters 'A' and 'B' respectively. Each plot has three contour lines; a dashed line for the relative decay rates β while the upper and the lower solid contour lines correspond to the error in decay rate ($\pm\Delta\beta$). Using the experimental values of γ from the Table T1, we obtained the relative decay rates β for the quantum emitters 'A' and 'B', as 0.818 ± 0.108 and 0.800 ± 0.124 respectively. From these simulations and the experimental values of β, it is evident that the quantum emitters are located within a narrow region at a distance $d \sim$21 nm from the surface of hBN/VO_2 interface. However, the uncertainty in the axial position depends on the emitters' polar angle θ. For emitter 'A', uncertainty (full width) varies from $\sim$13 nm at $\theta = 0°$ to $\sim$22 nm at $\theta = 90°$. Similarly, for quantum emitter 'B' uncertainty in their axial location varies from $\sim$ 15 nm to $\sim$23 nm at $\theta = 0°$ and $\theta = 90°$ respectively.

Next, we focus on emission polarimetry of the quantum emitters. Previous studies [50] have shown that the 3D orientation (θ, φ) of a dipole can be directly extracted by analyzing polarization characteristics of its emitted light. Figures 4(a), (b) is the emission polarization measurement from the quantum emitters 'A' and 'B' respectively. The data is fitted by the function [50]

$$I(\alpha) = I_{\min} + (I_{\max} - I_{\min})\cos^2(\alpha - \varphi), \qquad (2)$$

where $I_{\min,\ \max}$ and φ are the fitting parameters. From the fit, we obtained for emitter 'A': $I_{\min} = 0.356 \pm 0.013$, $I_{\max} = 0.966 \pm 0.024$ and $\varphi = 175.7° \pm 1.0°$. Similarly, for emitter 'B': $I_{\min} = 0.318 \pm 0.034$, $I_{\max} = 0.888 \pm 0.066$ and $\varphi = 109.9° \pm 2.9°$. In emission polarimetry, the polar angle θ can be extracted from the degree of polarization of the emission defined as

$$\delta(\theta) = \frac{I_{\max} - I_{\min}}{I_{\max} + I_{\min}}. \qquad (3)$$

From the fitting parameters ($I_{\max}$, $I_{\min}$), we obtained $\delta = 0.461 \pm 0.023$ and $\delta = 0.473 \pm 0.070$ for emitter 'A' and 'B' respectively. Figures 4(c) and (d) show the calculated degree of polarization δ as a function of the polar orientation angle θ using the experimental values of numerical aperture (0.9), the refractive indices of hBN, VO_2 (insulating phase) and sapphire. The distance d of the quantum emitters 'A' and 'B' from VO_2/sapphire substrate was set to $d \sim$ 21 nm. From figures 4(e) and (f) we clearly see that variation in the distance d is negligible (dashed line). The red dot in figures 4(e) and (f) represents the

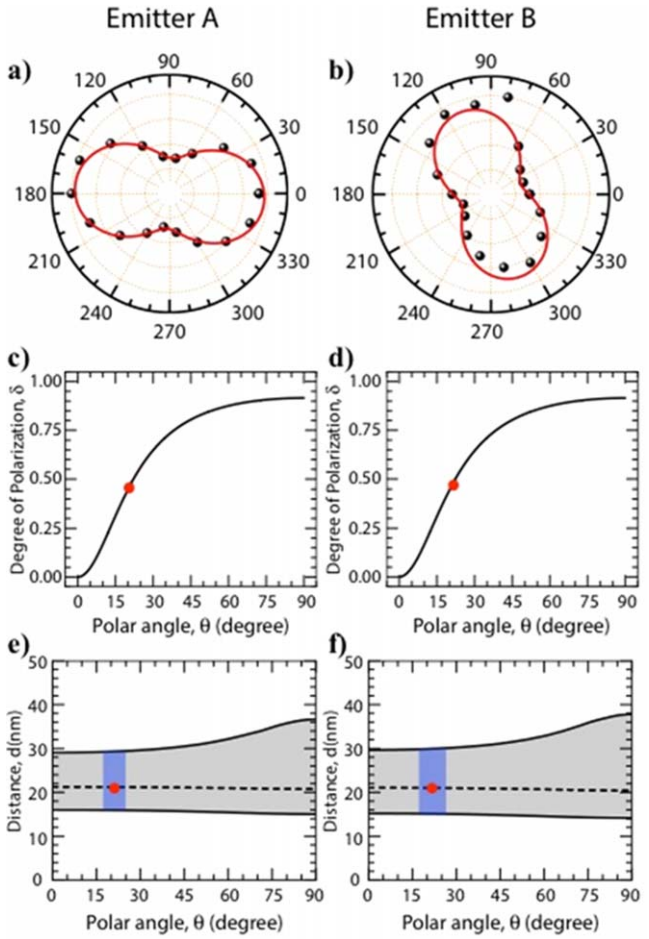

Figure 4. 3D-orientation of hBN quantum emitters and nanometric axial location. (a), (b) Polar plots of the photoluminescence (PL) intensity of the emitter 'A' and emitter 'B' respectively as a function of the emission polarization analysis angle (α). The PL data (solid spheres) were fitted using equation (2) to extract the azimuthal angle (φ) of the emitters and the degree of polarization (δ). From the fit, we deduce that for emitter A, $\varphi = 175.7° \pm 1.0°$; $\delta = 0.461 \pm 0.023$ and for emitter B, $\varphi = 109.9° \pm 2.9°$; $\delta = 0.473 \pm 0.070$. (c), (d) Calculated value of degree of polarization (δ) as a function of the polar angle (θ) of the emitters located at a distance of $\sim$ 21 nm from the surface of VO_2. The red dots in (c) and (d) corresponds to the experimental value of δ obtained from (a) and (b) respectively. The extracted value of the polar angle for emitter 'A' and 'B' are $\theta = 20.5° \pm 3.6°$ and $\theta = 21.2° \pm 4.5°$ respectively. (e), (f) Purple shaded region shows the range of the distance (d) and the polar angle (θ) of the emitters 'A' and 'B' respectively based on our experimental data and simulations.

measured value of δ and we extract the polar orientation angle $\theta = 20.5° \pm 3.6°$ and $\theta = 21.2° \pm 4.5°$ for emitter 'A' and 'B' respectively. In estimating the value of error in θ we accounted for the error in location d, which is shown figures 4(e) and (f) by solid lines. Figure 4(e) shows nanometer-scale axial localization of emitter 'A' with an uncertainty (full-width) of $\sim$ 15 nm, oriented along (θ, φ) = ($20.5° \pm 3.6°$, $175.7° \pm 1.0°$). Similarly, figure 4(f) shows nanometer-scale axial localization of emitter 'B' with an uncertainty full-width of $\sim$ 17 nm, oriented along (θ, φ) = ($21.2° \pm 4.5°$, $109.9° \pm 2.9°$). The strong vertical component of the dipole orientation for both emitters

found in the vicinity of hBN/VO_2 interface are consistent with our simulations results shown in figure S6. The predominant out of plane dipole orientation of these emitters can be a result of an out of plane atomic structure of the emitter as discussed in the literature [47, 51]. We believe the information provided by these measurements are of fundamental value in determining the underlying atomic structure of emitters.

Next, we investigated the feasibility of transferring the hBN flake from the VO_2 measurement substrate to a device substrate, which is a necessary capability for integration of quantum emitters with chip-based photonic components, waveguide circuits, and planar metamaterials [52–55]. In contrast to wet chemical transfer method [56], we utilized a polymer-assisted hot pickup technique [30, 57, 58] to transfer the emitter-host hBN flake from VO_2 to a receiving SiO_2/Si device substrate (supplementary figure S13). Figures 5(a), (b) show the optical image of the flake before and after the transfer. We were able to relocate the emitters 'A' and 'B' on the device substrate by performing confocal PL mapping (figure 5(c)) and matching the spectral (figure 5(d)) and spatial signatures of both emitters before and after the transfer process. We expect that the axial position of the emitters from the bottom surface and the polar angle of their dipole orientation to remain unchanged after the transfer. However, the azimuthal angle may change. Next, we performed emission polarimetry to determine the azimuthal angle of the emitters after the transfer. Figures 5(d) and (e) show polar plots of the PL intensity of the emitter 'A' and emitter 'B' respectively as a function of the emission polarization analysis angle (α). From the fit using equation (2), we deduce that for emitter A, $\varphi = 164.6° \pm 3.0°$ and for emitter B, $\varphi = 94.4° \pm 4.0°$. Next, we measured the relative orientation of the flake before and after the transfer. The transferred flake is oriented at an angle $\Delta\varphi = -12.6°$ with respect to its orientation on VO_2/sapphire which indicates that the azimuthal orientation of the emitters is also preserved within experimental errors.

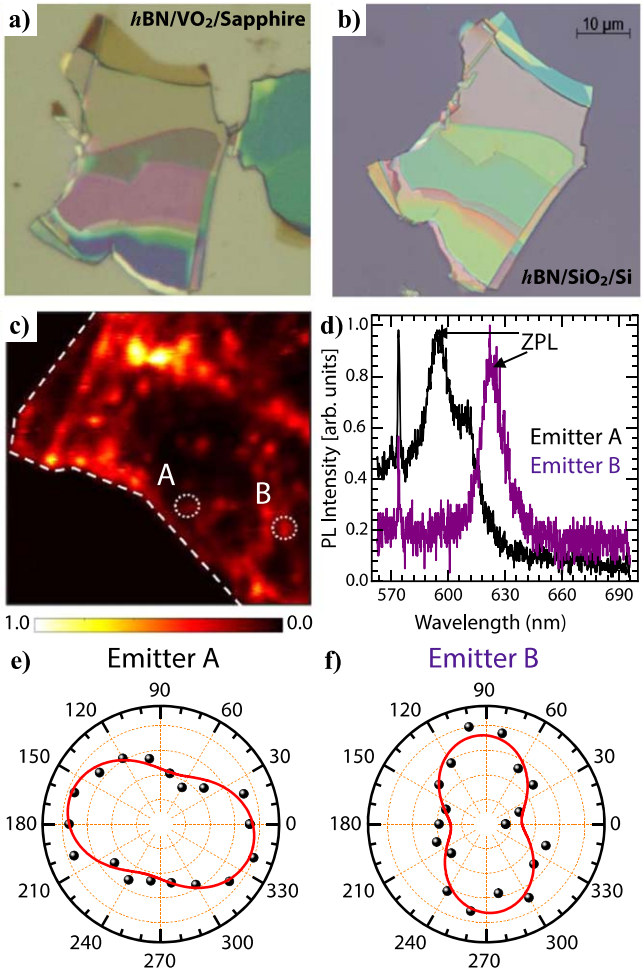

Figure 5. (a), (b) Optical image of the flake on VO_2/sapphire substrate (before transfer) and SiO_2/Si substrate (after transfer) respectively. The transferred flake is oriented at an angle $\Delta\varphi = -12.6°$ with respect to its orientation on VO_2/sapphire substrate. (c) Confocal photoluminescence (PL) map of the flake on SiO_2/Si substrate. Encircled (dashed white circle) highlights the region where emitters 'A' and 'B' are located. (d) PL spectra from the region highlighted in (c) shows the presence of emitters 'A' and 'B' which matched with the spectra obtained from the same location before transfer. The sharp line $\sim$ 575 nm corresponds to Raman line of hBN. (e), (f) Polar plots of the PL intensity of the emitter 'A' and emitter 'B' respectively as a function of the emission polarization analysis angle (α) on SiO_2/Si substrate after the transfer. From the fit using equation (2), we deduce that for emitter A, $\varphi = 164.6° \pm 3.0°$ and for emitter B, $\varphi = 94.4° \pm 4.0°$.

Conclusions

To summarize, we have demonstrated an experimental technique by which the axial position of quantum emitters in a multi-layered hBN flake can be extracted with nanometer-scale accuracy by exploiting the modification of photonic density of states using a phase change optical material, VO_2. Here, we tailor the optical environment of an emitter in the vicinity of VO_2/sapphire substrate which generates a sharply distance-dependent PL response. By performing time-resolved fluorescence spectroscopy, supplemented with emission polarimetry, several specific quantum emitters were identified at an axial distance of $\sim$ 21 nm from the hBN/VO_2 interface while also determining their full dipolar orientation (θ, φ). Although, in this work, we focused on locating hBN quantum emitters with ZPL in the wavelength range $\sim$ 550–640 nm, presence of other emitters with ZPL outside this range as well as embedded further deeper in the flakes cannot be ruled out. Next, we utilized a polymer-assisted hot pickup technique to transfer the identified hBN emitters from a VO_2 measurement substrate to a SiO_2/Si device substrate, which opens the door to coupling of fully characterized emitters, where each emitter has undergone precise measurement of axial position and orientation. It is worth noting that any phase-change material which experiences a sharp change in optical properties would be suitable for this purpose. However, VO_2 is particularly interesting because its insulator-to-metal transition happens near room temperature and is thus well suited to dynamically control emission rates of quantum emitters [59, 60] near room temperature. Owing to the broadband nature of change in the dielectric function of VO_2 when switched from the insulating to metallic phase, our technique could also be extended to locating other visible or

infrared quantum emitters [10]. Moving forward, characterizing and controlling the spectral diffusion of our localized *h*BN quantum emitters for generating identical photons would constitute an interesting direction for future research.

Experimental method

Optical characterization of samples was performed in a home-built confocal microscope capable of optical spectroscopy in visible range (Princeton HRS 300 system) and intensity autocorrelation measurement ($g_2(\tau)$) in a HBT configuration using a 50–50 beam splitter and two avalanche photo diodes (PDM Series-PicoQuant). We used a fast-scanning mirror (Newport) and a 4*f* telecentric configuration to perform photoluminescence mapping. The microscope uses a 532 nm CW laser (Cobolt) to pump emitters in *h*BN, a 100× objective (Leica) to focus the beam on the sample and used 50 μW power of laser (before objective) for all emitters. A quarter wave plate was put in the beam path at 45° orientations with respect to linear polarization of laser in order to produce circularly polarized light. We pumped with circularly polarized light to excite all emitters irrespective of their in-plane dipole orientation. A tunable bandpass filter (Semrock versachrome) was used to only pass the ZPL on the emitter into HBT setup to reduce background. Schematic of our optical characterization setup can be seen in figure S7. To measure the azimuthal component of the emitter's dipole orientation we put a rotating polarizer in the detection path via a flip mirror and we rotate the polarizer from a vertical configuration with increments of 20 degrees until 340 degrees and the intensity after the polarizer is recorded with an APD. A polar plot of intensity as a function of angle is plotted (figures 4(a), (b), 5(e), and (f)). Visibility of the polar plots were used to determine the polar component of the dipole orientation (figures 4(c) and (d)). Annealing in an inert environment is routinely used to create or activate quantum emitters in diamond as well as *h*BN. For the *h*BN samples described here, we annealed a bulk crystal of *h*BN at 950 °C in a 1 bar pressure argon gas for 30 min before exfoliation. We mounted our sample consisting of *h*BN/VO_2/sapphire on a Peltier heating stage.

Acknowledgments

We thank S Nam for the useful discussions. This work was supported by the DOE 'Photonics at Thermodynamic Limits' Energy Frontier Research Center under grant DE-SC0019140 and by the Boeing Company.

Data availability statement

The data that support the findings of this study are available upon reasonable request from the authors.

Author contributions

PKJ, HA, YK, and HAA conceived and developed the idea. PKJ prepared the *h*BN flakes and performed AFM measurements. HA performed the optical characterization of *h*BN flakes and correlation measurements. PKJ and HA performed emission polarimetry of *h*BN quantum emitters. YK prepared VO_2/sapphire sample; performed ellipsometry, full-wave simulations, optical, and AFM characterizations of VO_2 thin films. SB developed and performed transfer of *h*BN flake from VO_2/sapphire substrate onto SiO_2/Si for further studies. PKJ simulated the optical response of *h*BN quantum emitters and theoretical estimations with inputs from all co-authors. HAA supervised all the experiments, calculations, and data collection. All authors contributed to the data interpretation, presentation, and writing of the manuscript.

ORCID iDs

Pankaj K Jha https://orcid.org/0000-0002-5839-3391
Hamidreza Akbari https://orcid.org/0000-0002-6073-3885
Yonghwi Kim https://orcid.org/0000-0002-6652-7994
Souvik Biswas https://orcid.org/0000-0002-8021-7271
Harry A Atwater https://orcid.org/0000-0001-9435-0201

References

[1] Franklin A D 1972 *Point Defects in Solids* ed J H Crawford and L M Slifkin vol 1 (New York: Plenum Press) ch 1
[2] Nielsen M A and Chuang I L 2010 *Quantum Computation and Quantum Information* (Cambridge: Cambridge University Press)
[3] Weber J R, Koehl W F, Varley J B, Janotti A, Buckley B B, Van de Walle C G and Awschalom D D 2010 Quantum computing with defects *Proc. Natl Acad. Sci. USA* **107** 8513–8
[4] Beveratos A, Brouri R, Gacoin T, Villing A, Poizat J-P and Grangier P 2002 Single photon quantum cryptography *Phys. Rev. Lett.* **89** 187901
[5] Degen C L, Reinhard F and Cappellaro P 2017 Quantum sensing *Rev. Mod. Phys.* **89** 035002
[6] Doherty M W, Manson N B, Delaney P, Jelezko F, Wrachtrup J and Hollenberg L C L 2013 The nitrogen-vacancy colour centre in diamond *Phys. Rep.* **528** 1–45
[7] Awschalom D D, Hanson R, Wrachtrup J and Zhou B B 2018 Quantum technologies with optically interfaced solid-state spins *Nat. Photonics* **12** 516–27
[8] Kako S, Santori C, Hoshino K, Götzinger S, Yamamoto Y and Arakawa Y 2006 A gallium nitride single-photon source operating at 200 K *Nat. Mater.* **5** 887–92
[9] Morfa A J, Gibson B C, Karg M, Karle T J, Greentree A D, Mulvaney P and Tomljenovic-Hanic S 2012 Single-photon emission and quantum characterization of zinc oxide defects *Nano Lett.* **12** 949–54
[10] Aharonovich I, Englund D and Toth M 2016 Solid-state single-photon emitters *Nat. Photonics* **10** 631–41
[11] Atatüre M, Englund D, Vamivakas N, Lee S-Y and Wrachtrup J 2018 Material platforms for spin-based photonic quantum technologies *Nat. Rev. Mater.* **3** 38–51

[12] Srivastava A, Sidler M, Allain A V, Lembke D S, Kis A and Imamoğlu A 2015 Optically active quantum dots in monolayer WSe_2 *Nat. Nanotechnol.* **10** 491–6

[13] He Y-M *et al* 2015 Single quantum emitters in monolayer semiconductors *Nat. Nanotechnol.* **10** 497–502

[14] Koperski M, Nogajewski K, Arora A, Cherkez V, Mallet P, Veuillen J-Y, Marcus J, Kossacki1 P and Potemski1 M 2015 Single photon emitters in exfoliated WSe_2 structures *Nat. Nanotechnol.* **10** 503–6

[15] Chakraborty C, Kinnischtzke L, Goodfellow K M, Beams R and Nick Vamivakas A 2015 Voltage-controlled quantum light from an atomically thin semiconductor *Nat. Nanotechnol.* **10** 507–11

[16] Tonndorf P, Schmidt R, Schneider R, Kern J, Buscema M, Steele G A, Castellanos-Gomez A, van der Zant H S J, De Vasconcellos S M and Bratschitsch R 2015 Single-photon emission from localized excitons in an atomically thin semiconductor *Optica* **2** 347–52

[17] Tran T T, Bray K, Ford M J, Toth M and Aharonovich I 2016 Quantum emission from hexagonal boron nitride monolayers *Nat. Nanotechnol.* **11** 37–41

[18] Aharonovich I and Toth M 2017 Quantum emitters in two dimensions *Science* **358** 170–1

[19] Caldwell J D, Aharonovich I, Cassabois G, Edgar J H, Gil B and Basov D N 2019 Photonics with hexagonal boron nitride *Nat. Rev. Mater.* **4** 552–67

[20] Exarhos A L, Hopper D A, Grote R R, Alkauskas A and Bassett L C 2017 Optical signatures of quantum emitters in suspended hexagonal boron nitride *ACS Nano* **11** 3328–36

[21] Noh G, Choi D, Kim J-H, Im D-G, Kim Y-H, Seo H and Lee J 2017 Stark tuning of single-photon emitters in hexagonal boron nitride *Nano Lett.* **18** 4710–5

[22] Xia Y, Li Q, Kim J, Bao W, Gong C, Yang S, Wang Y and Zhang X 2019 Room-temperature giant stark effect of single photon emitter in van der waals material *Nano Lett.* **19** 7100–5

[23] Nikolay N, Mendelson N, Sadzak N, Böhm F, Tran T T, Sontheimer B, Aharonovich I and Benson O 2019 Very large and reversible stark-shift tuning of single emitters in layered hexagonal boron nitride *Phys. Rev. Appl.* **11** 041001

[24] Exarhos A L, Hopper D A, Patel R N, Doherty M W and Bassett L C 2019 Magnetic-field-dependent quantum emission in hexagonal boron nitride at room temperature *Nat. Commun.* **10** 222

[25] Gottscholl A *et al* 2020 Initialization and read-out of intrinsic spin defects in a van der Waals crystal at room temperature *Nat. Mater.* **19** 540–5

[26] Hayee F *et al* 2020 Revealing multiple classes of stable quantum emitters in hexagonal boron nitride with correlated optical and electron microscopy *Nat. Mater.* **19** 534–9

[27] Dietrich A, Doherty M W, Aharonovich I and Kubanek A 2020 Solid-state single photon source with fourier transform limited lines at room temperature. *Phys. Rev.* B **101** 081401(R)

[28] Tawfik S A, Ali A, Fronzi M, Kianinia M, Tran T T, Stampfl C, Aharonovich I, Toth M and Ford M J 2017 First-principles investigation of quantum emission from hBN defects *Nanoscale* **9** 13575–82

[29] Akbari H, Lin W-H, Vest B, Jha P K and Atwater H A 2021 Temperature-dependent spectral emission of hexagonal boron nitride quantum emitters on conductive and dielectric substrates *Phys. Rev. Appl.* **15** 014036

[30] Kang K, Lee K-H, Han Y, Gao H, Xie S, Muller D A and Park J 2017 Layer-by-layer assembly of two-dimensional materials into wafer-scale heterostructures *Nature* **550** 229–33

[31] Went C M, Wong J, Jahelka P R, Kelzenberg M, Biswas S, Hunt M S, Carbone A and Atwater H A 2019 A new metal transfer process for van der waals contacts to vertical Schottky-junction transition metal dichalcogenide photovoltaics *Sci. Adv.* **5** eaax6061

[32] Cai J-M, Retzker A, Jelezko F and Plenio M-B 2013 A large-scale quantum simulator on a diamond surface at room temperature *Nat. Phys.* **9** 168

[33] O'Brien J L, Furusawa A and Vučković J 2009 Photonic quantum technologies *Nat. Photonics* **3** 687–95

[34] Wehner S, Elkouss D and Hanson R 2018 Quantum internet: a vision for the road ahead *Science* **362** eaam9288

[35] Barnes W L, Horsley S A R and Vos W L 2020 Classical antennae, quantum emitters, and densities of optical states *J. Opt.* **22** 073501

[36] Drexhage K H 1974 *Progress in Optics* ed E Wolf (New York: Elsevier) vol XII, pp 163–232

[37] Jha P K, Mrejen M, Kim J, Wu C, Wang Y, Rostovtsev Y V and Zhang X 2016 Coherence-driven topological transition in quantum metamaterials *Phys. Phys. Lett.* **116** 165502

[38] Nalabothula M, Jha P K, Low T and Kumar A 2020 Engineering valley quantum interference in anisotropic van der Waals heterostructures *Phys. Rev.* B **102** 045416

[39] Ghosh A, Sharma A, Chizhik A I, Isbaner S, Ruhlandt D, Tsukanov R, Gregor I, Karedla N and Enderlein J 2019 Graphene-based metal-induced energy transfer for sub-nanometer optical localization *Nat. Photonics* **13** 860–5

[40] Qazilbash M M *et al* 2007 Mott transition in VO_2 revealed by infrared spectroscopy and nano-imaging *Science* **318** 1750–3

[41] Nikolay N, Mendelson N, Özelci E, Sontheimer B, Böhm F, Kewes G, Toth M, Aharonovich I and Benson O 2019 Direct measurement of quantum efficiency of single-photon emitters in hexagonal boron nitride *Optica* **6** 1084–8

[42] Stenzel O, Hahn J, Roder M, Ehrlich A, Prause S and Richter F 1996 The optical constants of cubic and hexagonal boron nitride thin films and their relation to the bulk optical constants *Phys. Status Solidi* a **158** 281–7

[43] Palik E D 1991 *Handbook of Optical Constants of Solids: Index* (Waltham, MA: Academic)

[44] Golla D, Chattrakun K, Watanabe K, Taniguchi T, LeRoy B J and Sandhu A 2013 Optical thickness determination of hexagonal boron nitride flakes *Appl. Phys. Lett.* **102** 161906

[45] Wigger D *et al* 2019 Phonon-assisted emission and absorption of individual color centers in hexagonal boron nitride *2D Mater.* **6** 035006

[46] Kianinia M, Regan B, Tawfik S A, Tran T T, Ford M J, Aharonovich I and Toth M 2017 Robust solid-state quantum system operating at 800 K *ACS Photonics* **4** 768–73

[47] Mendelson N *et al* 2021 Identifying carbon as the source of visible single-photon emission from hexagonal boron nitride *Nat. Mater.* **20** 321–8

[48] Wu E, Jacques V, Zeng H, Grangier P, Treussart F and Roch J-F 2006 Narrow-band single-photon emission in the near infrared for quantum key distribution *Opt. Express* **14** 1296–303

[49] Davis C C 2014 *Laser and Electro-optics: Fundamental and Engineering* (Cambridge: Cambridge University Press)

[50] Lethiec C, Laverdant J, Vallon H, Javaux C, Dubertret B, Frigerio J-M, Schwob C, Coolen L and Maître A 2014 Measurement of three-dimensional dipole orientation of a single fluorescent nanoemitter by emission polarization analysis *Phys. Rev.* X **4** 021037

[51] Lyu C, Zhu Y, Gu P, Qiao J, Watanabe K, Taniguchi T and Ye Y 2020 Single-photon emission from two-dimensional hexagonal boron nitride annealed in a carbon-rich environment *Appl. Phys. Lett.* **117** 244002

[52] Jha P K, Ni X, Wu C, Wang Y and Zhang X 2015 Metasurface-enabled remote quantum interference *Phys. Rev. Lett.* **115** 025501

[53] Jha P K, Shitrit N, Kim J, Ren X, Wang Y and Zhang X 2017 Metasurface-mediated quantum entanglement *ACS Photonics* **5** 971–6

[54] Jha P K, Shitrit N, Ren X, Wang Y and Zhang X 2018 Spontaneous exciton valley coherence in transition metal dichalcogenide monolayers interfaced with an anisotropic metasurface *Phys. Rev. Lett.* **121** 116102

[55] Ren X, Jha P K, Wang Y and Zhang X 2018 Non-conventional metasurfaces: from non-hermitian coupling, quantum interactions, to skin cloak *Nanophotonics* **7** 1233

[56] Vogl T, Campbell G, Buchler B C, Lu Y and Lam P K 2018 Fabrication and deterministic transfer of high-quality quantum emitters in hexagonal boron nitride *ACS Photonics* **5** 2305–12

[57] Pizzocchero F, Gammelgaard L, Jessen B, Caridad J M, Wang L, Hone J, Bøggild P and Booth T J 2016 The hot pick-up technique for batch assembly of van der Waals heterostructures *Nat. Commun.* **7** 11894

[58] Purdie D G, Pugno N M, Taniguchi T, Watanabe K, Ferrari A C and Lombardo A 2018 Cleaning interfaces in layered materials heterostructures *Nat. Commun.* **9** 5387

[59] Cueff S, Li D, Zhou Y, Wong F J, Kurvits J A, Ramanathan S and Zia R 2015 Dynamic control of light emission faster than the lifetime limit using VO_2 phase-change *Nat. Commun.* **6** 8636

[60] Szilard D, Kort-Kamp W J M, Rosa F S S, Pinheiro F A and Farina C 2019 Hysteresis in the spontaneous emission induced by VO_2 phase change *J. Opt. Soc. Am.* B **36** C46–51

[61] Kim Y, Wu P C, Sokhoyan R, Mauser K, Glaudell R, Shirmanesh G K and Atwater H A 2019 Phase modulation with electrically tunable vanadium dioxide phase-change metasurfaces *Nano Lett.* **19** 2961–3968

[62] Boll M K, Radko I P, Huck A and Andersen U L 2020 Photophysics of quantum emitters in hexagonal boron-nitride nano-flakes *Opt. Express* **28** 7475